Ti$_{12.5}$Zr$_{21}$V$_{10}$Cr$_{8.5}$Mn$_x$Co$_{1.5}$Ni$_{46.5-x}$ AB$_2$-type metal hydride alloys for electrochemical storage application: Part 1. Structural characteristics

L.A. Bendersky [a], K. Wang [a], I. Levin [a], D. Newbury [a], K. Young [b,*], B. Chao [b], A. Creuziger [a,c]

[a] *Material Measurement Laboratory, National Institute of Standards and Technology, Gaithersburg, MD 20899, USA*
[b] *Ovonic Battery Company, 2983 Waterview Drive, Rochester Hills, MI 48309, USA*
[c] *Kent State University, Kent, OH 44242, USA*

HIGHLIGHTS

► The secondary phases in AB$_2$-type MH alloy were studied by SEM, TEM, EBD, and EBSD.
► The solidification sequence of these secondary phases was identified.
► The composition and abundance of the final B2 phase were varied and analyzed.

ARTICLE INFO

ABSTRACT

The microstructures of a series of AB$_2$-based metal hydride alloys (Ti$_{12.5}$Zr$_{21}$V$_{10}$Cr$_{8.5}$Mn$_x$Co$_{1.5}$Ni$_{46.5-x}$) designed to have different fractions of non-Laves secondary phases were studied by X-ray diffraction, scanning electron microscopy, transmission electron microscopy, energy dispersive X-ray spectrometry, and electron backscatter diffraction. The results indicate that the alloys contain a majority of hydrogen storage Laves phases and a minority of fine-structured non-Laves phases. Formation of the phases is accomplished by dendritic growth of a hexagonal C14 Laves phase. The C14 phase is followed by either a peritectic solidification of a cubic C15 Laves phase (low Mn containing alloys) or a C14 phase of different composition (high Mn containing alloys), and finally a B2 phase formed in the interdendritic regions (IDR). The interdendritic regions may then undergo further solid-state transformation into Zr$_7$Ni$_{10}$-type, Zr$_9$Ni$_{11}$-type and TiNi-type phases. As the Mn content in the alloy increases, the fraction of the C14 phase increases, whereas the fraction of C15 decreases. In the IDRs when the alloy's Mn content increases the Zr$_9$Ni$_{11}$ phases and Zr$_7$Ni$_{10}$ phase fraction first increases and then decreases, while the TiNi-based phase fraction first increases and then stabilized at 0.02. IDR compositions can be generally expressed as (Ti,Zr,V,Cr,Mn,Co)$_{50}$Ni$_{50}$, which accounted for 7–10% of the overall alloy volume fraction.

1. Introduction

Transition metal-based AB$_2$ alloys, which exhibit high energy density and design flexibility, are candidates to replace rare earth-based AB$_5$ alloys currently used as metal hydride (MH) electrodes in nickel hydroxide/metal hydride (Ni/MH) batteries [1–5]. The AB$_2$ MH alloys are multi-element and multi-phase with a very high degree of local chemical disorder as pointed out by Ovshinsky et al. [1,6]. The large phase space and broad compositional range of these multi-component alloys allow flexibility in design, e.g. selectivity of the abundance of different phases and their morphologies.

Besides the majority C14 and C15 Laves phases, the alloys typically contain secondary phases such as TiNi, ZrNi, Zr$_7$Ni$_{10}$, Zr$_9$Ni$_{11}$, BCC, etc. [7–15]. These secondary phases are very crucial as catalysts for the proton diffusion and surface reaction under electrochemical environmental conditions [13–16]. In our recent publication the fine structure of the main Laves phases and the secondary phases was studied by transmission electron microscopy (TEM) and scanning electron microscopy (SEM) [17,18]. The phase formation process can be summarized as follows: (a) initial dendritic growth of a hexagonal C14 Laves phase followed by peritectic solidification of a cubic C15 Laves phase, (b) segregated interdendritic liquid solidifies as a cubic B2 phase, (c) solid-state transformation of the cubic B2 phase to Zr$_7$Ni$_{10}$-type and Zr$_9$Ni$_{11}$-type phases, as well as a martensitic bcc- or B2-related phase (Fig. 15 in Ref. 18). Subsequent X-ray diffraction (XRD) studies

* Corresponding author. Tel.: +1 248 293 7000; fax: +1 248 299 4520.
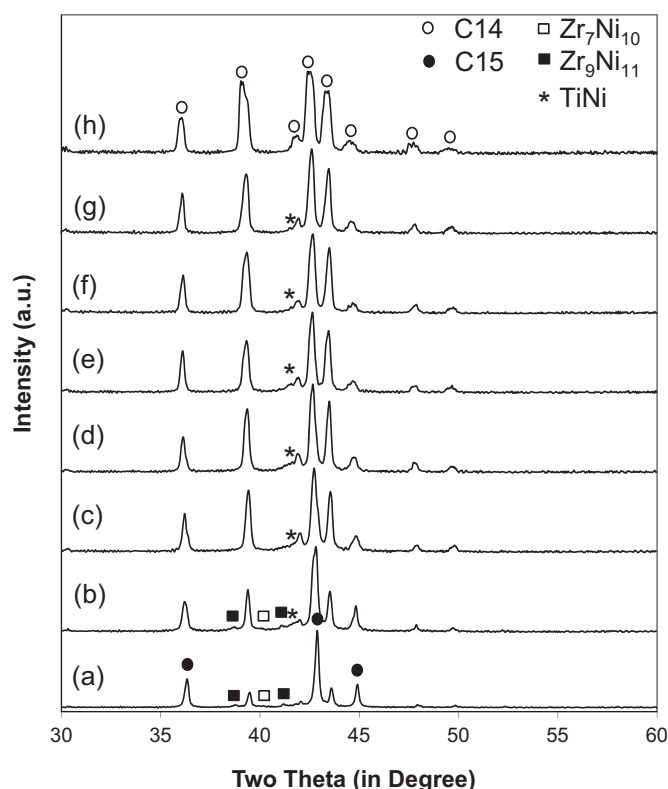 *E-mail address:* kyoung@ovonic.com (K. Young).

Fig. 1. XRD patterns using Cu K$_\alpha$ as the radiation source for alloys MN00 (a), MN01 (b), MN02 (c), MN03 (d), MN04 (e), MN05 (f), MN06 (g), and MN07 (h).

confirmed the possible presence of secondary phases closely related to the B2 TiNi- and ZrNi-types [19]. Since these secondary phases are very important for the electrochemical properties of the AB$_2$ MH alloys, this paper presents a detailed study of their fine structure. The correlations to both gaseous phase and electrochemical hydrogen storage characteristics will be discussed in Part 2 of this series of papers [20].

2. Experimental setup

A series of eight AB$_2$ seven-component alloys with varying Ni/Mn contents were designed for this study; the design assumes Zr and Ti on the A-sites (Zr + Ti = 33.5% atomic fraction, Zr/Ti = 1.68) and the remaining elements on the B-sites (V, Cr, Mn, Co, Ni, with Ni/Mn ratio varying from 16.9 to 0.97) of the Laves structure. Mn has very low solubility in Zr$_x$Ni$_y$ phases [16,21–23] and, therefore, higher Mn contents are expected to reduce the fractions of the Zr$_x$Ni$_y$ interdendritic phases. The target compositions together with the calculated average electron densities (e/a) for each alloy are listed in Table 1; the e/a ratio decreases with the increasing fraction of Mn (7 outer-shell electrons), which replaces Ni (10 outer-shell electrons). The e/a values correlate well with the relative fractions of the C14 and C15 phases [23,24]. For example, the AB$_2$ MH alloys suitable for Ni/MH applications are dominated by the C14 structure for e/a <6.9 and by the C15 structure for e/a >7.1. Thus, higher Mn contents are expected to promote the C14 phase and suppress the Zr$_x$Ni$_y$-type phases.

The alloy samples were prepared by arc melting under a continuous argon flow with a non-consumable tungsten electrode and a water-cooled copper tray. Before each arc melt, a piece of sacrificial titanium underwent a few melting–cooling cycles to reduce the residual oxygen concentration in the system. Each 10-g sample ingot was re-melted and turned over a few times to ensure

uniformity in chemical composition. The chemical compositions of the samples was examined by a Varian *Liberty* 100 inductively coupled plasma system[1] and were within 1% of the target values (Table 1). A Philips X'Pert Pro X-ray Diffractometer (XRD) was used for preliminary screening of the alloys' microstructure. Detailed XRD data suitable for Rietveld refinements were collected using a Panalytical X'Pert Pro diffractometer equipped with an incident beam monochromator (Cu Kα_1 radiation) and a Pixel position-sensitive detector. Rietveld refinements were performed using GSAS software. Elemental microanalysis was carried out with a Bruker "Quad SDD" silicon drift detector energy dispersive X-ray spectrometer (SDD-EDS) mounted on a JEOL8500F thermal field emission electron probe microanalyzer/scanning electron microscope. For Electron Backscatter Diffraction (EBSD) orientation and phase mapping, a Hitachi S4700 cold tip field emission scanning electron microscope (FE-SEM) was used. Oxford HKL Channel 5 software was used for EBSD acquisition and analysis. TEM investigations were carried out on Philips CM30 and JEM3010 microscopes operated at 200 kV and 300 kV, respectively. The TEM samples were prepared by embedding alloys in epoxy, thinning, mounting on a grid, dimpling and ion milling to perforation.

3. Results and discussion

3.1. Phase analysis by XRD study

XRD patterns for the eight alloys are shown in Fig. 1 and results are summarized in Table 1. The patterns are dominated by the peaks of the C14 phase; the peaks from C15 mostly overlap with those from C14. The fraction ratio for the C14 and C15 phases was estimated from the integrated intensities of the overlapped C14 and C15 peaks and the C14-only diffraction peaks using a calibration sample that contained a 1:1 mixture of the C14 and C15 phases. Lattice parameters of the C14 phase (Table 1) and the unit cell volume increase with the Mn content (the atomic radius of Mn is larger than that of Ni). Besides the main diffraction peaks of the C14 and C15 phases, a series of weak peaks attributed to Zr$_7$Ni$_{10}$-, Zr$_9$Ni$_{11}$-, and TiNi-type phases were observed. The volume/mass fractions of these minor phases were estimated from the integrated peak intensities; the fractions measured directly from SEM and TEM micrographs are comparable. As predicted by our design concept, the sum of Zr$_7$Ni$_{10}$ and Zr$_9$Ni$_{11}$ phase fractions decreases with increasing Mn content; concurrently, the fraction of TiNi-type increased for the first 5 alloys and then stabilized in the last 3 alloys.

Rietveld refinements of the X-ray diffraction data were performed for the alloys Mn00, Mn01, Mn04 and Mn07 (Fig. 2). The 2θ range included in the refinements was from 18° to 140°. Structural models for the C14 and C15 phases were constructed assuming Zr and Ti share the A-sites and the transition metals (V, Cr, Mn, Co and Ni) occupy the B-sites. The exact distribution of transition metals between the two non-equivalent B-sites in the C14 structure was not refined but the effects of this distribution on the refinements would likely to be small because the X-ray scattering factors for all of these elements are relatively similar. The X-ray profile coefficients for all the phases in a given sample were constrained to be equal.

The results of the Rietveld refinements in terms of constituent phase fractions and unit cell volumes are summarized in Table 2. Despite sample complexity, the simplified models provided satisfactory fits to the experimental data. A significant fraction of the C15 phase in both MN00 and MN01 samples is evident from the
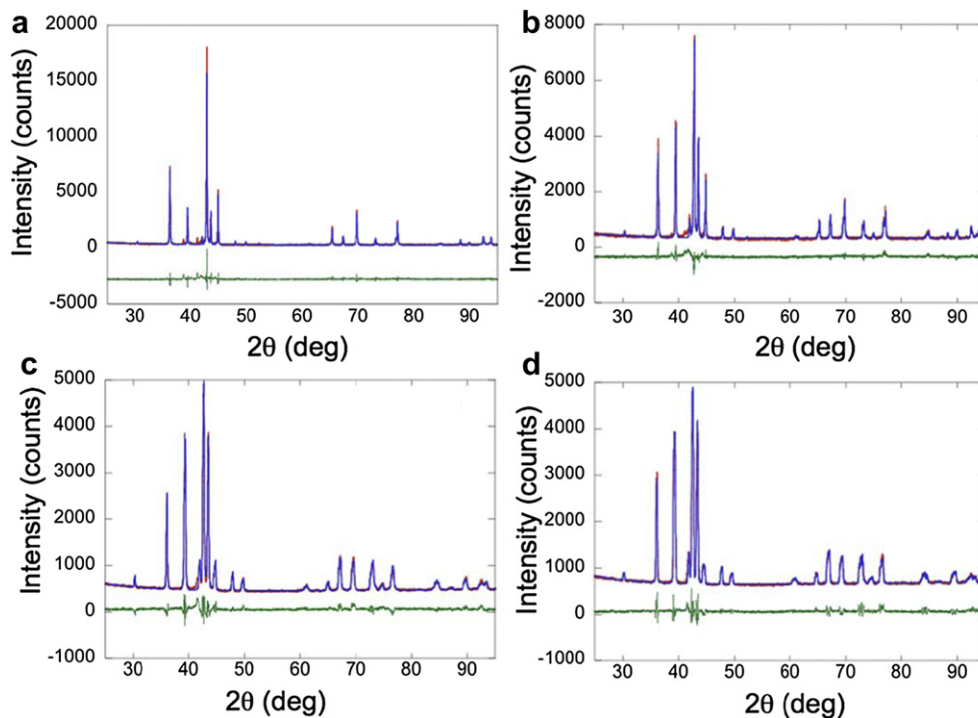
Fig. 2. Portions of experimental (red) and fitted (blue) X-ray diffraction profiles for the MN00 (a), MN01 (b), MN04 (c), and MN07 (d) samples. The phase assemblages used to obtain the fitted profiles are summarized in Table 1. The fitting agreement factors were $R_{wp} = 8.9\%$, $\chi^2 = 3.6$ for MN00; $R_{wp} = 7.48\%$, $\chi^2 = 2.5$ for MN01; $R_{wp} = 4.19\%$. $\chi^2 = 1.03$; and $R_{wp} = 3.35\%$, $\chi^2 = 1.02$ for MN07. [For interpretation of the references to colour in this figure legend, the reader is referred to the web version of this article.]
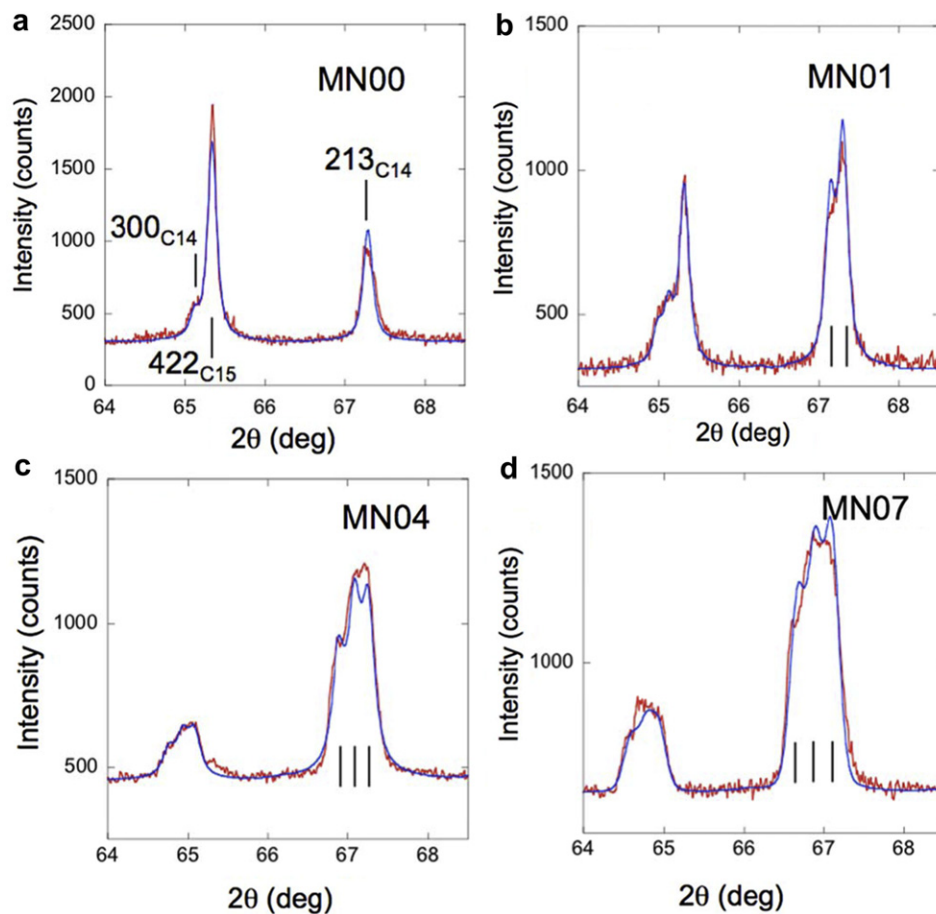

Fig. 3. Magnified view of selected C14/C15 reflections in the MN00 (a), MN01 (b), MN04 (c), and MN07 (d) samples. Experimental and fitted profiles are indicated using red and blue colors, respectively. [For interpretation of the references to colour in this figure legend, the reader is referred to the web version of this article.]
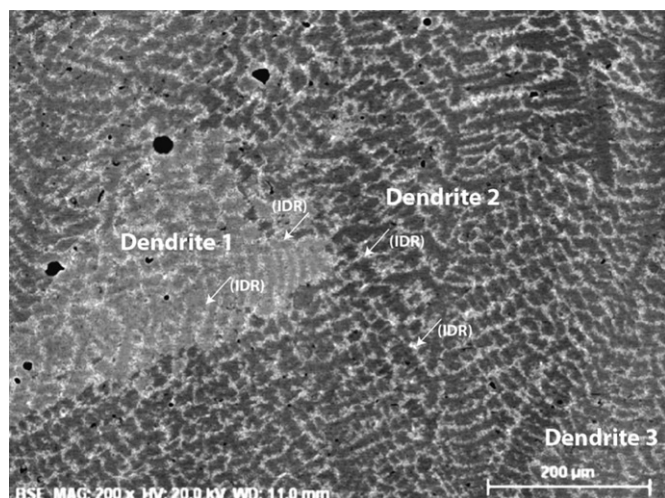
Fig. 4. A low magnification BSE image of the MN02 alloy showing several dendrites separated by boundaries that includes interdendritic regions (IDR).

relatively sharp C15 peaks (Fig. 3a and b); the presence of C15 in these samples was further ascertained by the presence of several weak but well-separated C15 reflections. The number of C14 phase components is evident from the splitting of certain Bragg reflections (Fig. 3). For example, a 213 peak of the C14 structure, while already distorted in the MN00 sample, splits into a well-resolved doublet in the MN01 sample, which signifies the presence of the two C14 phases with distinct compositions. This peak further splits into three components in the MN04 sample and becomes even more distorted in the MN07 sample. The results clearly show that the alloys consist of a number of distinct C14 phases rather than a single phase with a broad distribution of d-spacings, which might be expected for typical compositional variations in the cast structure (coring). Use of a high-resolution powder diffractometer was critical for resolving these multiple C14 phases.

3.2. Microstructures observed by SEM/EDS

The microstructure and elemental composition of the four alloys MN01−MN04 that contained a mixture of the C14 and C15 phases (Tables 1 and 2) were examined using SEM and SDD-EDS. Fig. 4 is a low magnification SEM backscattered electron (BSE) image of the MN02 alloy; the image shows a dendritic cast structure and is typical of all of the studied alloys. Large dendrites are seen clearly; the impinging secondary arms of the dendrites are separated by the boundaries along which interdendritic regions (IDR) are located. Fig. 5 shows higher magnification BSE images (first column), which reveal more details of the IDRs; contrast variations inside the dendrites are a combination of chemical and orientation differences. The IDRs have concave boundaries, which suggests that these regions are the last to solidify pockets of a residual melt.

Fig. 5a presents SDD-EDS maps of Ti K$_\alpha$ (the second column) and Cr K$_\alpha$ (the third column) characteristic intensities from the same BSE-imaged regions. These elemental maps clearly show that the IDRs are Ti-rich and Cr-deficient relative to the dendrites. The dendrites consist of two compositionally distinct regions: region D1 in a dendrite core (Ti-deficient and Cr-rich relative to the average dendrite composition) and region D2 (Ti-rich and Cr-deficient) surrounding D1; the regions are labeled in Fig. 5b. Fig. 5b shows a higher magnification view the Ti K$_\alpha$ map for the MN02 sample; the interfaces between IDR and D2 are rather sharp, whereas those between D1 and D2 are somewhat diffuse. The

average compositions of these regions, which were determined from measurements at several locations, are summarized in Tables 3−5. Compositions of regions D1 and D2 can be formulated according to AB$_2$ stoichiometry of Laves phases as following: D1 = (Ti + Zr)$_{0.32}$(V + Cr + Mn + Co + Ni)$_{0.68}$ and D2 = (Ti + Zr)$_{0.345}$(V + Cr + Mn + Co + Ni)$_{0.655}$; that is, the measured compositions are consistent with Laves structures. The compositions of both the D1 and D2 regions become enriched in Mn and depleted in Ni from Mn01 to Mn04, which concurs with changes in the overall compositions of these alloys.

Volume and mass fractions of the regions/phases were calculated from areas of different intensities in the Ti K$_\alpha$ maps and from the redistribution of the average composition into local compositions, respectively (Tables 3−5). Our initial assumption, which was validated in the previous work on a similar class of alloys [17], would be that the D1 and D2 regions consist of distinct cubic C15 and hexagonal C14 Laves phase polytypes; however, in the present case, such an intuitive assumption is only partially consistent with the XRD data. The results of compositional and XRD measurements can be reconciled (Tables 1 and 2) by assuming that the D1 and D2 regions crystallize with the individual C14 structures identified via Rietveld analysis as exhibiting distinct compositions and, therefore, distinct lattice parameters. The compositional differences for the two C14 phases are maintained (within the error of EDS measurements) for all four alloys (MN01−MN04) (Table 6). The primary difference in the composition of the two regions is in the Ni concentration (atomic fraction 9−12%). Only the MN01 alloy exhibits differences in the Zr, V and Cr contents, which is probably consistent with the fact that the C15 phase is present in this sample.

EDS measurements of the IDR compositions are summarized in Table 5. The IDR compositions for the four alloys are similar and can be approximated as (Ti,Zr,V,Cr,Mn,Co)$_{50}$Ni$_{50}$, which suggest formation of an AB phase (either TiNi or ZrNi type). Overall, the IDR compositions for the different alloys have approximately constant contents of Ti (atomic fraction 24%), Zr (atomic fraction 20%), Cr (atomic fraction 0.5%), Co (atomic fraction 1%) and Ni (atomic fraction 50%), and become depleted in V and enriched in Mn with increasing alloys' Mn concentration. The volume fractions of the IDR regions range from 7% to 10%.

Close examination of the IDRs revealed that they consist of grains having a complex internal sub-structure rather than a single phase. Fig. 6 shows BSE images of the IDRs for the four alloys studied; all images show the presence of elongated particles (EPs) embedded in a matrix. The EPs are aligned in two directions that appear to be orthogonal (the observed different orientations are in fact assemblages of particles of the same orientation). The length of the EPs ranges from less than 2 μm to 0.1 μm, and the width is typically less than 0.1 μm. The number density of the EPs inside the IDRs is not uniform; among the four alloys examined by SEM/EDS, the highest number density is in MN01 and the lowest is in MN04. Fig. 7 shows the BSE image of another IDR of the MN01 alloy. The image shows a bright region surrounding the IDR grain; similar bright intensity was observed for a few particles inside the IDR grain. EDS analysis using a small-size probe was obtained from various locations in Fig. 7, and the results are listed in Table 7. SD is the main AB$_2$ Laves phase. Attempts to measure the compositions of the EP and the matrix (IGP and IGM in Table 7) were unsuccessful − despite different contrast of these components, their measured compositions were similar and close to the average composition of IDR. However, the bright region labeled as PP in Fig. 7 yielded a composition with atomic fraction 57% Ni − significantly higher than the average Ni content (atomic fraction 50%)(see Table 7). Similar Ni-rich compositions were measured for an area near PP and for a few blocky particles inside the IDR (marked as 1, 2, 4, 5).
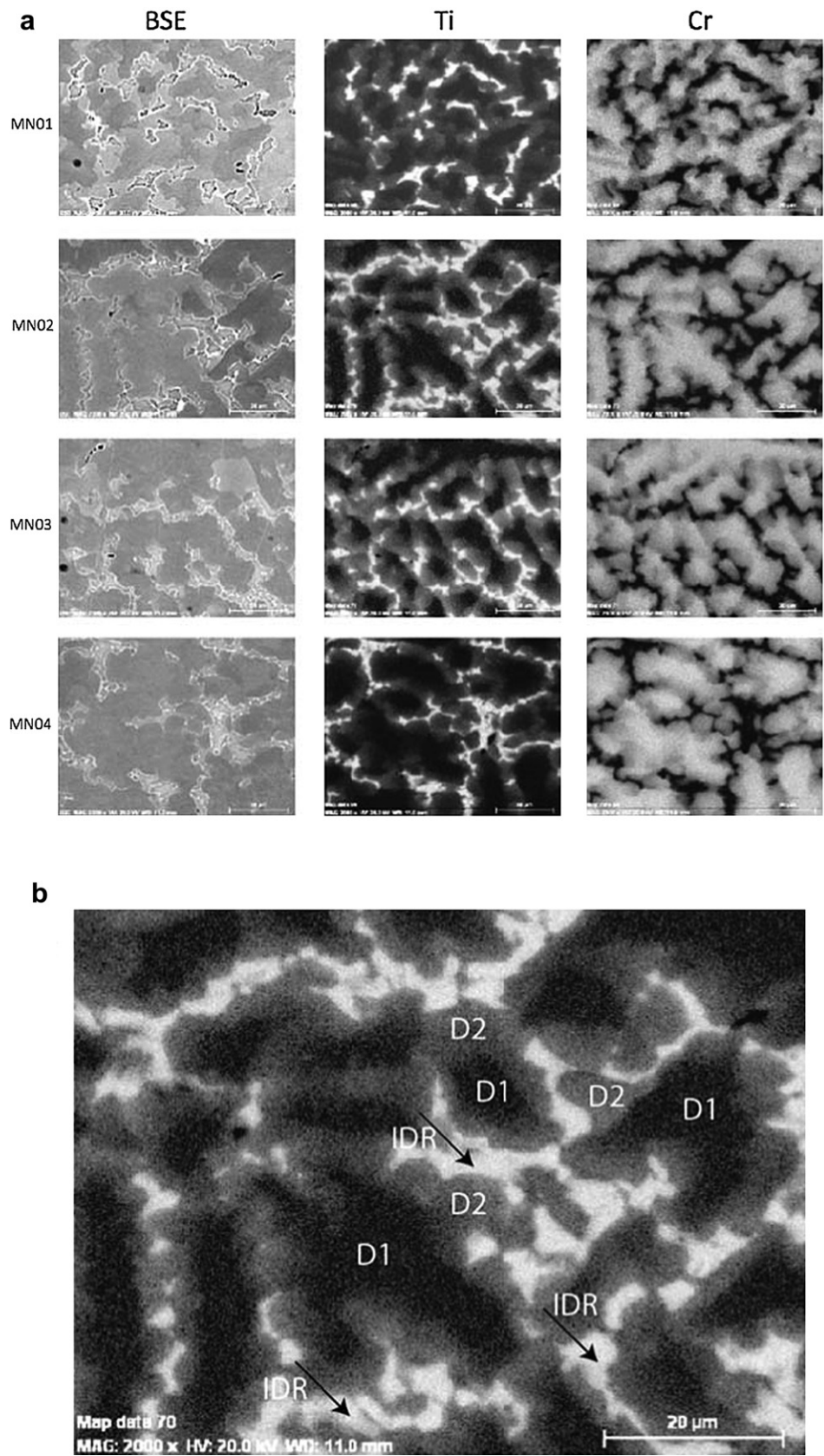
Fig. 5. (a) Backscattered SEM and compositional EDS maps using Ti K$_\alpha$ and Cr K$_\alpha$ for four alloys. (b) Enlarged Ti K$_\alpha$ map showing Ti-rich interdendritic regions (IDR), Ti-lean central part of dendrites (D1) and outer dendritic regions containing intermediate concentrations of Ti (D2).
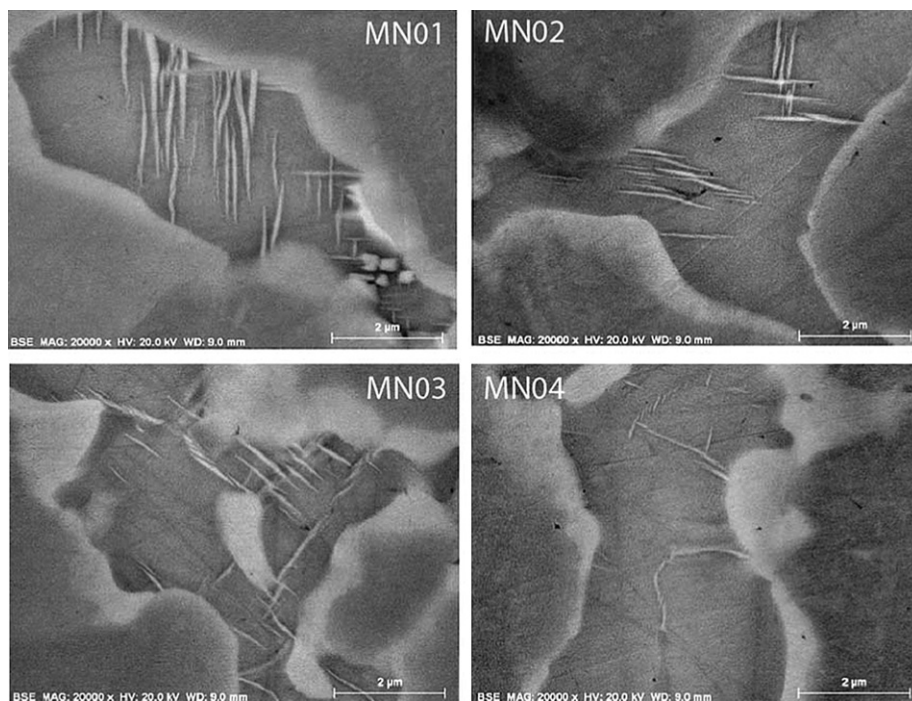
Fig. 6. BSE images of interdendritic grains for four MN01–MN04 alloys.

The composition can be presented as $(Zr,Ti)_{40}(V,Cr,Mn,Co)_3Ni_{57}$, which is very close to the stoichiometry of Zr_7Ni_{10}.

3.3. Microstructures observed by EBSD

Samples MN01 and MN04 were investigated with EBSD to measure the fractions of different Laves phases and their distribution. The EBSD technique has been explained in detail in Ref. [25]. In short, a scanning electron beam strikes an inclined (typically 70°) sample surface and the diffraction patterns featuring Kikuchi bands from the backscattered electrons are recorded. These diffraction bands are then automatically indexed to determine crystallographic nature and orientation of a grain. Examples of Kikuchi patterns for the C14 and C15 phases from sample MN01 are shown

Fig. 7. BSE images of interdendritic grains for four MN01–MN04 alloys. Numbers on the image represent points from which EDS compositions (Table 7) were measured.

in Fig. 8; selected poles from the calculated crystallographic orientation are superimposed on the Kikuchi patterns. To facilitate phase-distribution mapping, the crystal structures of the C14 phase ($P6_3/mmc$, $a = 4.98$ Å, $c = 8.12$ Å) and C15 phase ($Fd\overline{3}m$, $a = 6.957$ Å) were used [26]. Between 8 and 11 diffraction bands were used to determine the phase and its orientation. Square grids of 50 by 50 points with a step size of 1 μm were used for the maps.

The areas investigated in samples MN01 and MN04 are shown in Fig. 9a and b, respectively. These images are created using fore-scatter detectors mounted near the phosphor screen and are similar to backscattered images. The contrast in these images is affected by an average atomic number, sample orientation, and surface topography. Overlaid on these images are the color phase maps. Red colored points represent the C15 phase identified by EBSD analysis; blue points correspond to the C14 phase. The points for which indexing was not possible are left transparent. Due to the fairly small area of points in the map and the possible presence of the B2 phase, no attempt was made to identify their structure. The non-indexed points likely belong to either the interdendritic regions (B2-based fine phases) or severely distorted regions near grain boundaries.

In Fig. 9a, the structure of the dendrites is recognizable for the sample MN01; along the center of the dendrite (diagonal in the image) the hexagonal phase is predominant. Closer to the dendrite edges and along the interdendritic regions, the cubic C15 phase appears. In contrast, the sample MN04 has a very small fraction of the cubic phase regions (Fig. 9b). Some sections of the dendritic structure could not be indexed (lower left quadrant in Fig. 9b), possibly because of either the high number of bands required for phase identification or slightly different lattice parameters of the C14 phase in these regions (Table 2).

The XRD, EBSD and SEM results can be summarized as follows: (1) the C14 phase is the first to crystallize and form dendrites; (2) at the later crystallization stage, a secondary dendritic phase envelops the dendritic arms of the primary C14 phase; (3) the secondary phase is the C15 Laves phase for the alloys with lower Mn content
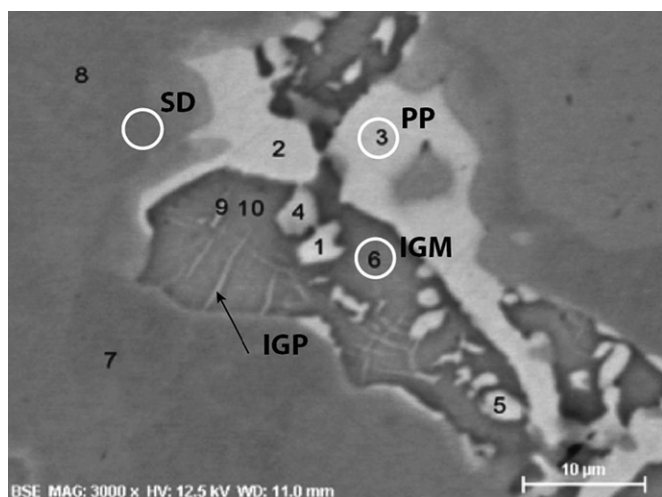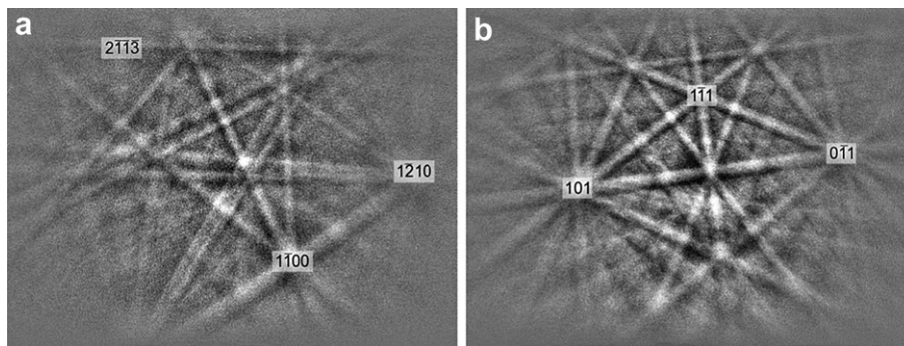
Fig. 8. Kikuchi diffraction patterns for hexagonal C14 phase (a) and cubic C15 phase (b). Both patterns are from sample MN01. Orientation data from automatic indexing of the Kikuchi patterns are shown for selected poles.

and/or the second C14 phase of a different composition for the higher Mn containing alloys; (4) the IDRs region contains the last phase to solidify and have approximately average compositions AB; and (5) the crystallized IDR phase undergoes a solid-state transformation.

3.4. Microstructures observed by TEM

TEM studies of four alloys (MN01–MN04) were performed to clarify the XRD/SEM results and to obtain additional structural information on the Laves and IDR phases. Fig. 10a shows a low magnification bright field TEM image from the MN01 sample where an IDR grain (labeled as B2) is surrounded by dendritic grains. The IDR grains can be recognized by their mostly concave boundaries (a manifestation of their being the final portion of the melt to solidify), internal fine structure, and electron diffraction patterns with strongest reflections corresponding to B2. In Fig. 10a the IDR grain is surrounded by a distinct layer identified by selected area electron diffraction (SAED) as a cubic C15 Laves phase (Fig. 10b). The C15 phase is also in contact with another phase identified by SAED as hexagonal C14 (Fig. 10c). The C14 and C15 phases are in the orientation relationship (OR) $\{111\}\langle 110\rangle_{C15}//\{0001\}\langle 11\bar{2}0\rangle_{C14}$; this OR established from SAED in Fig. 10d reflects the fact that the difference between the structures of C14 and C15 lies in the different stacking of the same structural blocks [26]. This and similar images confirm the solidification sequence for the low Mn alloys as C14 → C15 → B2.

Based on the XRD measurements, it is expected that the IDR grains would be in direct contact with the C14 phase for the samples with higher Mn; indeed Fig. 11 shows a TEM image from the MN04 sample where an IDR grain (labeled as B2) is surrounded by the grains of the C14 structure. In contrast to the MN01 samples,

the C14 phase in higher Mn samples typically contains a high density of defects that were identified as dislocation walls separating misoriented cells (Fig. 12a). The C15 phase present in samples containing higher concentrations of Mn features planar (111) stacking faults and twins (Fig. 12b); a corresponding SAED pattern (inset of the photo) was indexed as the fcc C15 with two sets of planar {111} twins and stacking faults contributing to the diffuse intensity streaks. The differences in the type of extended defects in the C15 and C14 phases provide robust fingerprints for distinguishing these phases in TEM samples without composition or diffraction measurements. Considering the poor statistics of the selected TEM observations of a coarse cast structure, the conclusion that the presence of defects correlates with Mn content should be seen as tentative; the appearance of the dislocation defects could be strongly affected by the variation of thermal stresses, while formation of twins and stacking faults depends on local compositional variations.

As is evident from the complex diffraction contrast of IDRs in Figs. 10 and 11, the grains consist not of a single phase but rather a fine-scale complex microstructure. The scale of the microstructure suggests a post-solidification solid-state transformation as its origin. The elongated particles seen in the BSE images of Fig. 6 are shown by TEM to be in orthogonal directions of the cubic axes (Fig. 13a), suggesting that the uniform matrix observed between the EPs via BSE imaging in fact consist of agglomerates of very fine particles. The IDR grain shown in Fig. 13b consists entirely of such fine microstructure without EPs; visibility of the fine microstructure strongly depends on the grain orientation (diffraction conditions).

SAED from the IDR grains of all the studied alloys yields average cubic symmetry manifested in intense reflections of the ordered B2 structure ($a \approx 3.0$ Å) and additional weaker reflections that have a complex ordered distribution obeying the cubic symmetry.
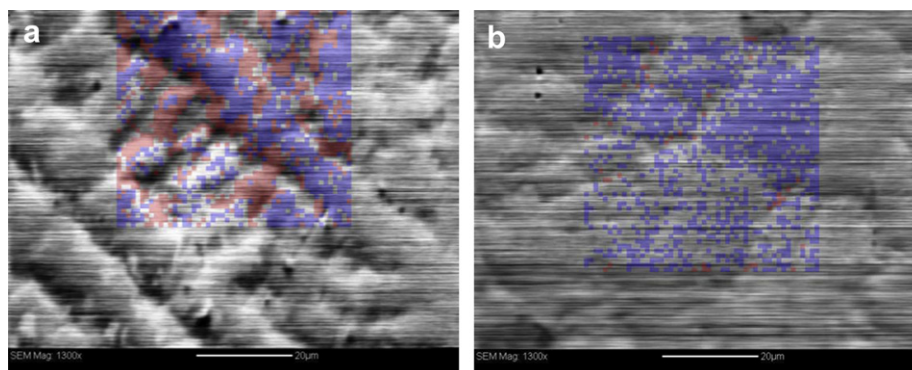

Fig. 9. EBSD phase ID maps overlaid on forescatter detector images for sample MN01 (a) and MN04 (b). Red indicates cubic C15 phase, blue indicates hexagonal C14 phase. Non-indexed points are transparent. [For interpretation of the references to colour in this figure legend, the reader is referred to the web version of this article.]
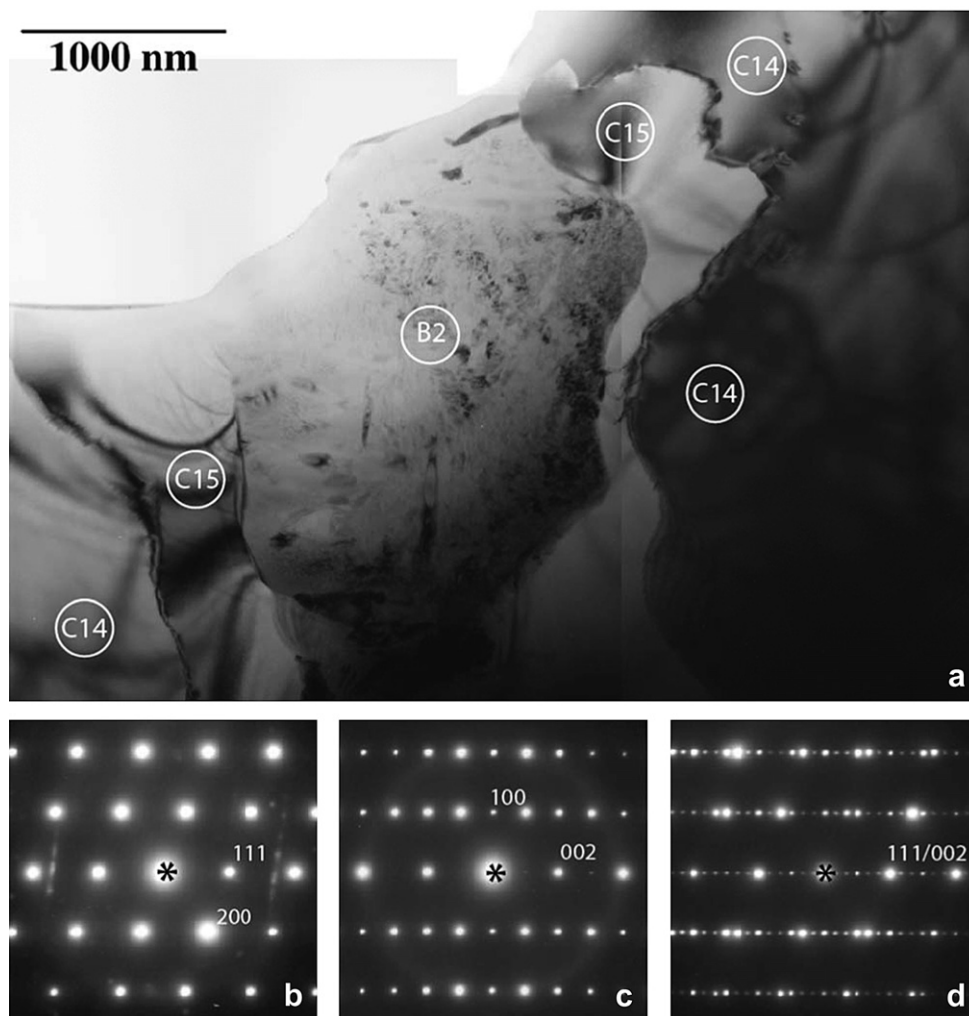
Fig. 10. (a) A low magnification bright field TEM image from the MN01 sample showing an interdendritic region (labeled B2) surrounded by dendritic C15 and C14 Laves phases. The phases are identified by SAED − [011] zone axis of C15 (b) and [1−10] of C14 (c). (d) SAED pattern from both C15 and C14 phases from which the orientation relationship was derived. Streak-like features in (b) come from the neighboring interdendritic grain.

Similar SAED patterns were observed for the alloy studied in our previous publication [18]. According to that work, the weaker reflections belong to different low-temperature phases and their

Fig. 11. A bright field TEM image from the MN04 sample where an IDR grain (labeled as B2) is surrounded by grains of the C14 structure.

structural variants exhibit an orientation relationship with a cubic lattice. We have identified the following major phases: an orthorhombic Zr_7Ni_{10}-type phase and a phase that according to $\mathbf{k} = 1/3(110)^*_{B2}$ reflections and $\{110\}_{B2}$ stacking faults was suggested to be a close-packed martensite. Occasionally, the tetragonal Zr_9Ni_{11}-type phase was also observed. SAED patterns from IDRs of all the studied alloys are nearly identical; in Fig. 14, examples of the $\langle 001 \rangle_{B2}$-type patterns for the three different alloys are shown. The $\langle 001 \rangle_{B2}$ patterns have strong reflections (or rather a cluster of reflections) indexed as the cubic B2 and symmetrically arranged groups of weaker reflections around ½ ½ 0 (encircled in Fig. 14). The weaker reflections maintain the same positions but their intensities vary even within the same IDR grain; these intensity variations are attributed to variable volume fractions of constituent phases and their orientational variants. Since IDRs in all the studied alloys exhibit similar compositions (only slight variations in V, Mn and Ni contents, see Table 5), we infer that they always crystallize as a cubic B2 phase and then undergo the same solid-state phase transformation(s).

Analysis of the $\langle 001 \rangle_{B2}$ pattern shows that part of the observed reflections can be attributed to the two orthogonal variants of the Zr_7Ni_{10}-type phase in $[011]_{Zr7Ni10}$ orientation, Fig. 15a. These variants contribute rows of ½ 100_{B2} reflections in $\langle 100 \rangle^*$ directions. For

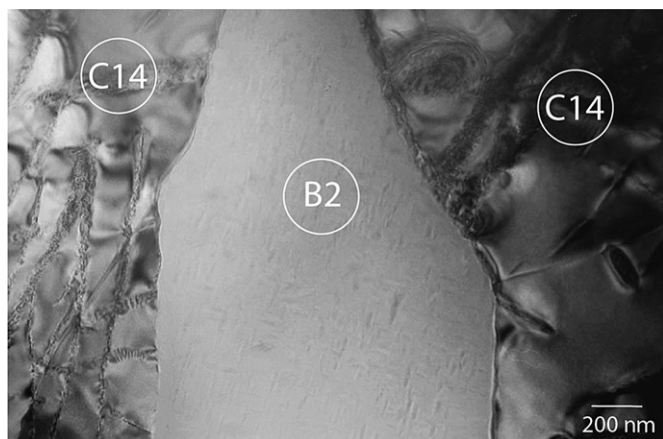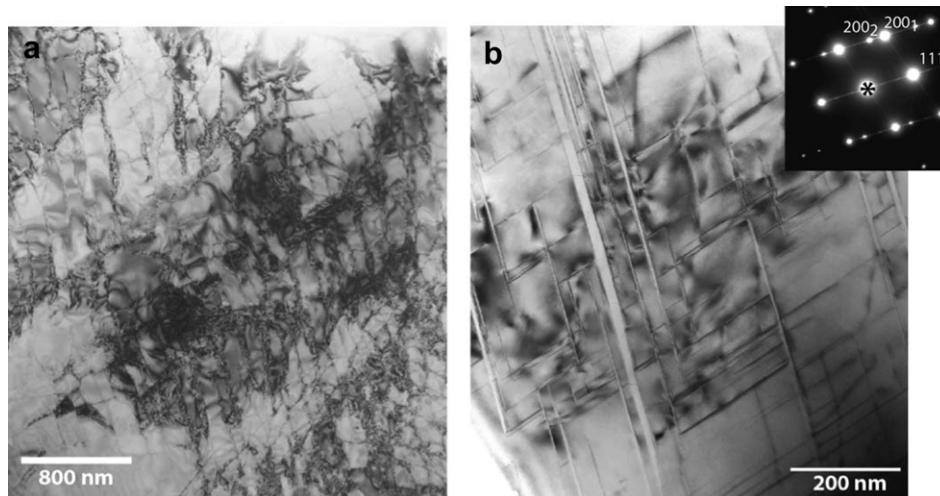**Fig. 12.** Bright field TEM image from MN02 (a) and MN03 (b) samples showing the internal structure of a C14 grain, with high dislocation density and low angle boundaries, and stacking faults and twins in a C15 grain, respectively.
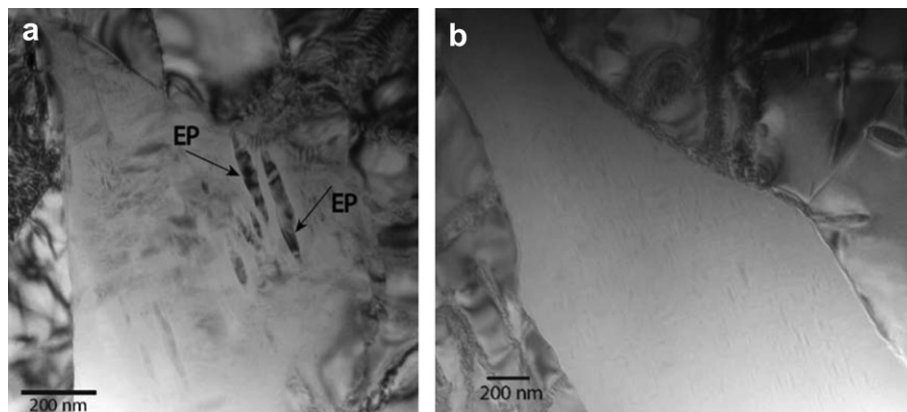

Fig. 13. Bright field TEM images of interdendritic grains from the MN04 alloy.

a good fit, lattice parameters of the binary Zr_7Ni_{10} [27] have to be modified to $a = 12.38$ Å; $b = 8.55$ Å; $c = 8.63$ Å (b and c parameters are shorter by 6% than the corresponding parameters in Zr_7Ni_{10}). Dark field imaging indicates that the two variants of Zr_7Ni_{10} belong to the separate orthogonal lenticular-shape particles, e.g. in Fig. 16a and b, which is consistent with the TEM images in Figs. 16 and 17 in Ref. [18]. By symmetry, the OR between Zr_7Ni_{10} and B2 produces six orientational variants.

The remaining reflections in the $\langle 001 \rangle_{B2}$ patterns can be accounted for by the two orthogonal variants of a phase with 1/3

$\{011\}_{B2}$ rows of reflections, Fig. 15b. Tilting the IDR grains to $\langle 111 \rangle_{B2}$ reveals that in many grains three (or four) variants are intermixed. Our previous paper has suggested that the phase with the 1/3 $\{011\}_{B2}$ reflections is a close-packed martensitic phase based on the B2 structure; such martensitic phases were observed, e.g., for NiTi and crystallographically can be considered as different shuffling sequences of $\{110\}_{B2}$ planes [28]. The dark field image in Fig. 16c recorded using 1/3$\{110\}_{B2}$ reflections shows that this phase forms lenticular particles. Tilting around the $\langle 110 \rangle^*_{B2}$ axis from $\langle 001 \rangle_{B2}$ to $\langle 111 \rangle_{B2}$ orientations shows a very complex distribution of

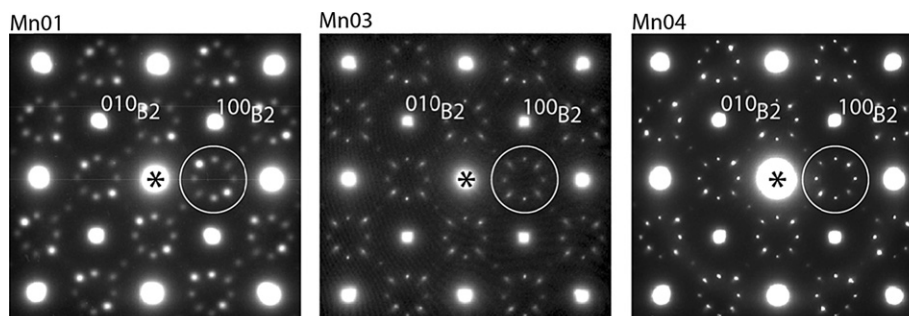**Fig. 14.** Comparison of [001]$_{B2}$-type SAED patterns for MN01 (a), MN03 (b) and MN04 (c) alloys.
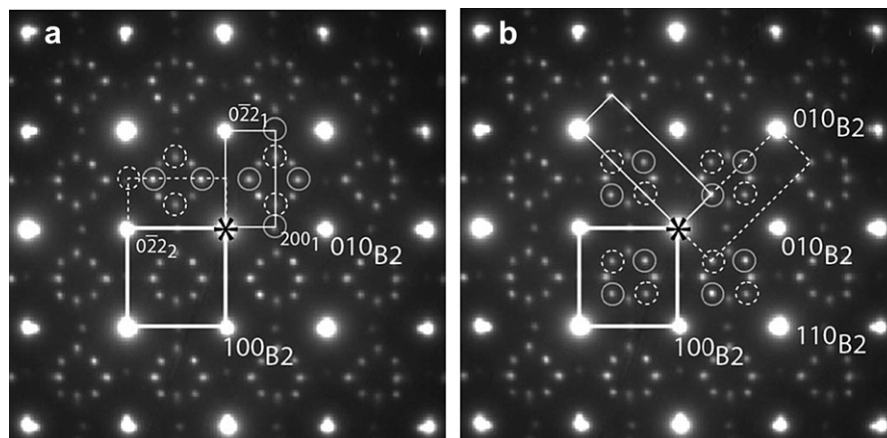
Fig. 15. Analysis of $[001]_{B2}$-type SAED patterns. (a) The encircled reflections forming a cross around $\frac{1}{2}(100)_{B2}$ center are indexed as belonging to two variants of Zr_7Ni_{10}. (b) Remaining reflections of the $1/3\langle110\rangle$-type forming a 90-degree rotated cross are identified as belonging to a different phase. Reflections of different variants are distinguished by using circles with dash and full lines.

Table 1
Design composition and phase abundances (mass fraction) estimated from XRD patterns, Fig. 1.

Alloy	Ti (at.%)	Zr (at.%)	V (at.%)	Cr (at.%)	Mn (at.%)	Co (at.%)	Ni (at.%)	e/a	C14 phase (%)	C15 phase (%)	Zr_7Ni_{10} phase (%)	Zr_9Ni_{11} phase (%)	TiNi phase (%)
MN00	12.5	21.0	10.0	8.5	2.6	1.5	43.9	7.06	34	49	2	15	0
MN01	12.5	21.0	10.0	8.5	5.6	1.5	40.9	6.97	65	23	4	7	1
MN02	12.5	21.0	10.0	8.5	8.6	1.5	37.9	6.88	85	8	4	1	2
MN03	12.5	21.0	10.0	8.5	11.6	1.5	34.9	6.79	90	4	3	0	3
MN04	12.5	21.0	10.0	8.5	14.6	1.5	31.9	6.70	89	4	2	1	4
MN05	12.5	21.0	10.0	8.5	17.6	1.5	28.9	6.61	97	0	1	0	2
MN06	12.5	21.0	10.0	8.5	20.6	1.5	25.9	6.52	97	0	1	0	2
MN07	12.5	21.0	10.0	8.5	23.6	1.5	22.9	6.43	98	0	0	0	2

reflections, Fig. 17. Additionally, the periodicity of $\{110\}_{B2}$ planes is $12 \times d_{\{110\}B2}$ (second and third SAED pattern in Fig. 17). Further work is in progress to establish the crystal structure of this phase.

3.5. Discussion

A combination of SEM/EDS, EBSD, XRD and TEM was required to establish correlation between the alloys composition and the changes in distribution and morphology of the phases in these multi-component, multi-phase alloys. The results demonstrate that the cast alloys have a major dendritic structure of Laves phases, with a minority of phases located in the interdendritic regions. The

dendrites consist of a core having a C14 hexagonal Laves phase; the phase shows almost no coring (compositional spread), probably because of its stoichiometric nature. At some point of growth, the core dendrite phase switches to a secondary Laves phase of a different composition. This secondary phase crystallizes with a C15 cubic phase for the alloys with Mn <8.6 at.% and Ni >38 at.% (MN00 and MN01). For the alloys with Mn >8.6 at.% and Ni <38 at.% (MN02 through MN07), the second dendritic phase crystallizes with a C14 structure having a composition different from that of a core (Table 6). XRD results suggest that the dendrites consist of more than two distinctive C14 phases for higher Mn-content alloys. The experimental results suggest the multi-component Ti–Zr–Mn–TM–Ni phase diagram has multiple isolated single-phase regions of AB_2 stoichiometry that are in equilibrium with the melt.

Growth of the second dendritic phase is topotactic [29] for both C14 and C15 phases, with an uninterrupted orientation relationship for $(0001)_{C14}/(111)_{C15}$ planes. The C14/C14′ interface is clearly seen

Table 2
Results of phase analyses in Mn-substituted Laves phase samples using Rietveld refinements. The numbers in parenthesis represent estimated standard deviations in refined parameters as calculated by GSAS. The actual uncertainties are likely to be larger being dominated by systematic errors that are difficult to quantify (i.e. uncertainties in phase compositions or element partitioning among atomic crystallographic positions). C14-1, C14-2 and C14-3 are phases with the C14 structure but with different lattice parameters and compositions.

Alloy	Phases	Phase fraction	Phase volume, Å³
MN00	C14	0.50 (1)	172.24 (1)
MN00	C15	0.50 (1)	341.86 (1)
MN00	C14-1	0.49 (1)	172.21 (1)
MN01	C14-2	0.32 (1)	173.30 (1)
MN01	C15	0.19 (1)	342.22 (1)
MN01	C14-1	0.39 (1)	172.56 (1)
MN04	C14-2	0.39 (1)	173.77 (1)
MN04	C14-3	0.22 (1)	175.20 (1)
MN07	C14-1	0.39 (1)	173.73 (1)
MN07	C14-2	0.36 (1)	175.25 (1)
MN07	C14-3	0.25 (1)	176.76 (1)

Table 3
Compositions (in at.%) of a core dendritic phase D1. Volume fraction of the phase was estimated from its area fraction in Ti K_α maps. Mass fraction of the phase was estimated from the deviation from the alloy's nominal composition. For each alloy the composition is an average of 10 measurements.

Alloy	Ti	Zr	V	Cr	Mn	Co	Ni	Volume/mass fraction From compos., %	From maps, %
MN01	10.1	22.1	14.4	9.6	7.6	1.9	34.4	38	28.70
MN02	9.8	22.4	14.4	8.5	12.0	1.9	31.0	31	21.39
MN03	10.0	22.5	13.6	8.5	15.3	1.8	28.4	34	23.61
MN04	9.8	22.9	13.0	9.4	18.6	1.7	24.5	33	27.97

Table 4
Compositions (in at.%) of a secondary dendritic phase D2. Volume fraction of the phase was estimated from its area fraction in Ti K_α maps. Mass fraction of the phase was estimated from the deviation from the alloy's nominal composition. For each alloy the composition is an average of 10 measurements.

Alloy	Ti	Zr	V	Cr	Mn	Co	Ni	Volume/mass fraction	
								From compos., %	From maps, %
MN01	13.2	21.9	8.4	3.5	5.1	1.5	46.3	57	63.46
MN02	12.7	21.6	11.1	4.0	9.3	1.6	40.0	62	68.31
MN03	13.1	21.3	10.7	4.2	11.8	1.6	37.4	62	67.03
MN04	14.3	20.7	9.8	3.8	13.6	1.5	36.2	69	65.45

Table 6
Difference in composition between D1 and D2 phases (Δ = D2−D1).

Alloy	Ti	Zr	V	Cr	Mn	Co	Ni
MN01	3.1	0.8	−6.0	−6.1	−2.5	−0.4	11.9
MN02	2.9	−0.8	−3.3	−4.5	−2.7	−0.3	9
MN03	3.1	−1.2	−2.9	−4.3	−3.5	−0.2	9
MN04	4.5	−2.2	−3.2	−5.6	−5.0	−0.2	11.7

in composition maps for the MN02–04 alloys, especially for Ti K_α, (Fig. 5); however the interface is not visible in TEM images. The C14/C15 interface in TEM is recognized by the change in diffraction from hexagonal to cubic while in the images the interface exhibits an array of interfacial dislocations.

The presence of the secondary, non-Laves phases in these alloys are essential for the performance of Ni–MH batteries, as they provide extra catalytic capability through synergetic effects [13–16]. Thus, knowledge of phase composition, morphology, and dispersion of the constituent phases is important. In the studied cast alloys, the secondary phase, being the last portion of the melt to solidify, is dispersed between dendritic arms of the Laves phase. Compositional maps of the alloys in Fig. 5 suggest connectivity between the IDRs and thus the presence of a secondary-phase network. Thus the effect of IDRs on hydrogenation is not only due to the particles distributed on the electrode surfaces but also those dispersed though the bulk. The composition of the IDRs remains almost the same for different alloys, with a slight increase in Mn and decrease in V observed for higher Mn alloys; the composition can be approximated as binary $(Zr,Ti,V,Cr,Mn,Co)_{50}Ni_{50}$, which suggests crystallization in the form of the TiNi-type B2 structure. The average cubic symmetry of the diffraction patterns from IDRs, with strong clusters of reflections situated at the positions of B2 ($a \approx 3.0$ Å), is another strong suggestion that IDRs crystallize as a high-temperature B2 phase.

TEM of the IDRs showing a very complex structure of tightly-packed fine lenticular particles with well-defined orientation relationship to an underlying cubic lattice is clear evidence of a solid-state transformation from the high-temperature B2 to the structurally related lower-temperature phases. Size, morphology, and multiple crystallographic variants related by cubic symmetry all indicate that the solid-state transformation had occurred under conditions of limited long-range diffusion. The larger, elongated particles were identified as the Zr_7Ni_{10}-type phase by SAED and exhibiting a Ni content that was 50 at.% higher than that observed in the "matrix", Table 7. As the temperature of a cast sample decreases on cooling, and the composition of the matrix changes with the ensuing precipitation, the condition for diffusionless transformation at lower temperatures is reached. Thus the B2

matrix transforms to a coordinated arrangement of a different variant of a martensitic phase. The martensitic transformation was studied for the B2 TiNi compounds, as well as for off-stoichiometric compounds and those substituted with different transition metals, as reported previously [30]. The martensite phase belongs to a family of close-packed structures formed from a bcc or bcc-ordered B2 by displacements (shuffle) and distortions of the {011} crystallographic planes. Different sequences of displacements with overlying chemical AB order of B2 can produce a variety of crystal structures, e.g. the most studied 3R and 9R [31].

Both Zr–Ni and martensitic phases can have an effect on the hydrogenation properties of Laves-based alloys. The effects of non-Laves secondary phases on the electrochemical properties were studied before [16]. Zr_9Ni_{11} and TiNi phases were found to increase the electrochemical storage capacities, degrade the half-cell high-rate dischargeability, and improve both charge retention and cycle life. ZrNi and Zr_7Ni_{10} phases work in the opposite manner. The difference between the hydrogenation properties of austenitic and martensitic phases has been also studied for $Ti_{50-x}Zr_xNi_{50}$ alloy with ($0 < x < 24$) [32]. The study found that the martensitic structure is able to store a much higher amount of hydrogen than the austenitic one. Zr_7Ni_{10}-type and martensitic phases appear as a mixture in the studied alloys, and their relative volume fractions vary depending on the local cooling conditions and compositional variations.

4. Summary

A series of AB$_2$-based metal hydride alloys ($Ti_{12.5}Zr_{21}V_{10}Cr_{8.5}Mn_xCo_{1.5}Ni_{46.5-x}$) designed to contain different ratios of the non-Laves secondary phase by varying Mn/Ni content were studied. As the Mn content in the alloy increases, the fraction of the C14 phase increases, whereas the fraction of C15 decreases. In IDRs, with increase of the alloy's Mn content, the Zr_9Ni_{11} phases and Zr_7Ni_{10} phase fraction first increases and then decreases, while the TiNi-based phase fraction first increases and then stabilized at 0.02, although variations in local conditions may significantly vary the numbers. The morphologies, compositions, and crystallographic orientations of constituent phases indicate that during cooling from liquid, a core C14 phase was solidified first, followed by a second C14 phase (in the case of high Mn alloys) or a C15 phase (in the case of low Mn alloy), forming a dendritic structure. The interdendrite region is occupied by the last-to-solidify B2 phase, which undergoes further solid-state transformation into Zr_7Ni_{10}-, Zr_9Ni_{11}-, and TiNi-type phases.

Table 5
EDS composition measurements of interdendritic regions (IDR) (in at.%) and estimation of its volume (using area measurement) and mass (from compositions of phases) fraction.

Alloy	Ti	Zr	V	Cr	Mn	Co	Ni	Mass/volume fraction	
								From compos., %	From maps, %
MN01	23.2	20.5	2.0	0.6	1.8	1.0	50.8	5	7.84
MN02	23.0	20.2	1.7	0.4	2.8	1.0	50.3	7	10.30
MN03	23.5	20.3	1.8	0.5	3.6	0.8	49.2	4	9.36
MN04	24.1	19.5	1.5	0.4	4.2	1.0	49.2	8	6.58

Table 7
Compositions (in at.%) of different components in IDR of MN01 (see Fig. 7).

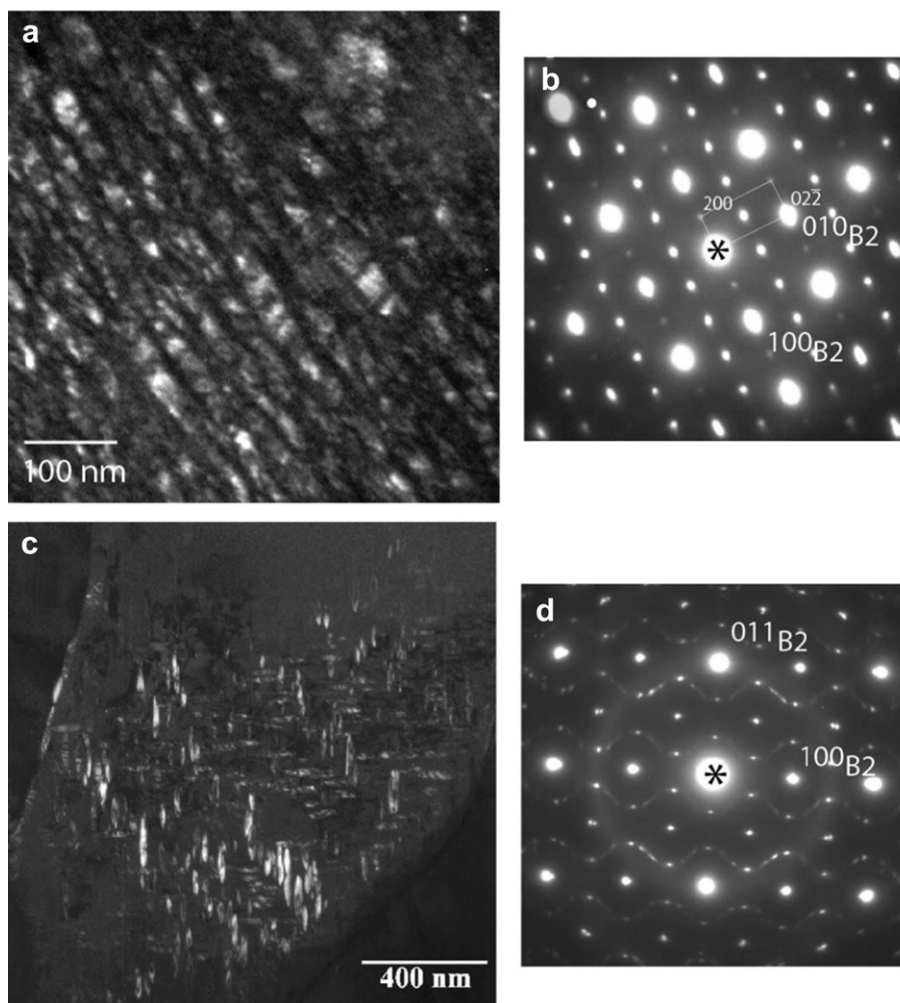| Location	Ti	Zr	V	Cr	Mn	Co	Ni
D1	10.1	22.1	14.4	9.6	7.6	1.9	34.4
D2	13.2	21.9	8.4	3.5	5.1	1.5	46.3
IDR (average)	23.2	20.5	2.0	0.6	1.8	1.0	50.8
PP	15.4	25.2	1.1	0.28	0.95	0.6	56.4
IGM	24.9	19.2	1.8	0.4	2.1	1.1	50.2
IGP	23	19.7	1.6	0.4	1.7	1.0	52.4
SD	12	21.8	11.0	5.5	6.0	1.7	41.0

Fig. 16. Dark field images of an IDR grains obtained by using reflections of Zr_7Ni_{10}-type phase in $[001]_{B2}$ orientation (a,b) and martensitic phase in $[011]_{B2}$ orientation.
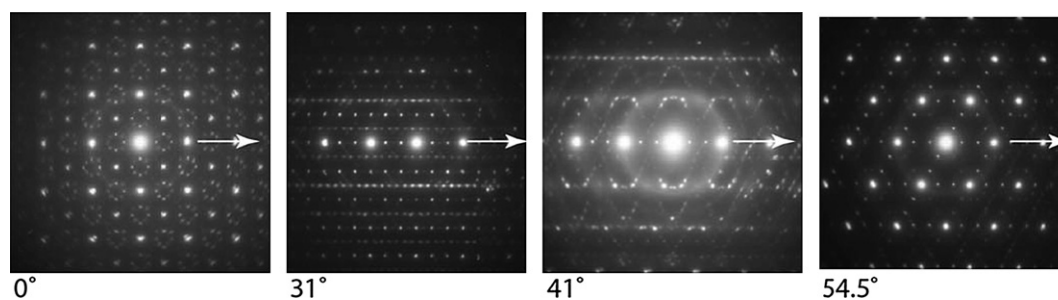

Fig. 17. A series of SAED patterns obtained from an IDR grain of Mn01 samples by tilting around $[110]_{B2}$ axis.

Acknowledgement

References

[1] S.R. Ovshinsky, M.A. Fetcenko, J. Ross, Science 260 (1993) 176.
[2] M.A. Fetcenko, S.R. Ovshinsky, K. Young, B. Reichman, C. Fierro, J. Koch, F. Martin, W. Mays, T. Ouchi, B. Sommers, A. Zallen, J. Alloys Compd. 330–332 (2002) 752.
[3] K. Young, M.A. Fetcenko, C. Fierro, in: Proceedings of 2011 IEEE Power & Energy Society General Meeting, July 24–29, 2011, Detroit, USA, IEEE, New York, USA, 2011.
[4] M.A. Fetcenko, Proceedings of Pacific Power Source Symposium 2011, Jan. 10–14, 2011, Hawaii, USA.
[5] M.A. Fetcenko, Proceedings of 28th International Battery Seminar & Exhibit, Mar. 14–17, 2011, Fort Lauderdale, Florida, USA.
[6] K. Sapru, B. Reichman, A. Reger, S.R. Ovshinsky, US Patent 4,623,597 (1986).
[7] J.M. Joubert, M. Latroche, A. Percheron-Guégan, J. Alloys Compd. 231 (1995) 494.
[8] J.M. Joubert, M. Latroche, A. Percheron-Guégan, J. Bouet, J. Alloys Compd. 240 (1996) 219.
[9] J.M. Joubert, D. Sun, M. Latroche, A. Percheron-Guégan, J. Alloys Compd. 253 (1997) 564.
[10] W.K. Zhang, C.A. Ma, X.G. Yang, Y.Q. Lei, Q.D. Wang, Trans. Nonferrous Met. Soc. China 19 (1999) 505.

[11] Q.A. Zhang, Y.Q. Lei, X.G. Yang, K. Ren, Q.D. Wang, J. Alloys Compd. 292 (1999) 236.
[12] J.C. Sun, S. Li, S.J. Ji, J. Alloys Compd. 404–406 (2005) 687.
[13] F.C. Ruiz, E.B. Castro, S.G. Real, H.A. Peretti, A. Visintin, W.E. Triaca, Int. J. Hydrogen Energy 33 (2008) 3576.
[14] A. Visintin, H.A. Peretti, F. Ruiz, H.L. Corso, W.E. Triaca, Alloys Compd. 428 (2007) 244.
[15] F.C. Ruiz, E.B. Castro, H.A. Peretti, A. Visintin, Int. J. Hydrogen Energy 35 (2010) 9879.
[16] K. Young, T. Ouchi, B. Huang, B. Chao, M.A. Fetcenko, L.A. Bendersky, K. Wang, C. Chiu, J. Alloys Compd. 506 (2010) 841.
[17] W.J. Boettinger, D.E. Newbury, K. Wang, L.A. Bendersky, C. Chiu, U.R. Kattner, K. Young, B. Chao, Metall. Mater. Trans. A 41 (2010) 2033.
[18] L.A. Bendersky, K. Wang, W.J. Boettinger, D.E. Newbury, K. Young, B. Chao, Metall. Mater. Trans. A 41 (2010) 1891.
[19] K. Young, J. Nei, T. Ouchi, M.A. Fetcenko, J. Alloys Compd. 509 (2011) 2277.
[20] K. Young, B. Chao, L.A. Bendersky, K. Wang, J. Power Sources 218 (2012) 487–494.
[21] N.W.M. Ritchie, Microsc. Today 19 (2011) 30.
[22] K. Young, T. Ouchi, Y. Liu, B. Reichman, W. Mays, M.A. Fetcenko, J. Alloys Compd. 480 (2009) 521.
[23] K. Young, T. Ouchi, M.A. Fetcenko, W. Mays, B. Reichman, Int. J. Hydrogen Energy 34 (2009) 8695.
[24] K. Young, T. Ouchi, B. Huang, J. Nei, M.A. Fetcenko, J. Alloys Compd. 501 (2010) 236.
[25] B.S. Chao, R.C. Young, S.R. Ovshinsky, D.A. Pawlik, B. Huang, J.S. Im, B.C. Chakoumakos, in: D. Doughty, L. Nazar, M. Arakawa, H.-P. Brack, K. Naoi (Eds.), New Materials for Batteries and Fuel, Mater. Res. Soc. Symp. Proc., vol. 575, 1999, p. 193. Warrendale, PA.
[26] O. Engler, V. Randle, Introduction to Texture Analysis: Macrotexture, Microtexture and Orientation Mapping, second ed., CRC Press, 2010.
[27] J.M. Joubert, R. Cerny, K. Yvon, M. Latroche, A. Percheron-Guegan, Acta Cryst. C 53 (1997) 1536.
[28] K. Otsuka, X. Ren, Prog. Mater. Sci. 50 (2005) 511.
[29] L.S.D. Glasser, F.P. Glasser, H.F.W. Taylor, Q. Rev. Chem. Soc. 16 (1962) 343.
[30] K. Otsuka, X. Ren, Mat. Sci. Eng. 89 (1999) A273.
[31] L. Delaey, M. Chandrasekaran, J. Phys. IV 05 (1995) C2–251.
[32] F. Cuevas, M. Latroche, P. Ochin, A. Dezellus, J. Fernandez, C. Sanchez, A. Percheron-Guegan, J. Alloys Compd. 330–332 (2002) 250.